Journal of Alloys and Compounds 1036 (2025) 181720

Contents lists available at ScienceDirect

Journal of Alloys and Compounds

journal homepage: www.elsevier.com/locate/jalcom

Fast synthesis of biocompatible iron oxide nanoparticles via a microwave-assisted Schikorr reaction: Phase-director influence of iron glycinate complexes

Antonio Santana-Otero [a,1], Carlos Frade-González [b,c,1], Milagrosa Ramírez-del-Solar [b,d], Daniel Ortega [b,c,e,*]

[a] Institute of Materials Science of Madrid (ICMM-CSIC), Sor Juana Inés de la Cruz 3, Madrid 28049, Spain
[b] Condensed Matter Physics department, Faculty of Sciences, Campus Universitario de Puerto Real, Puerto Real, Cádiz 11510, Spain
[c] Biomedical Research and Innovation Institute of Cádiz (INiBICA), Cádiz 11009, Spain
[d] Institute of Research on Electron Microscopy and Materials, University of Cádiz (IMEYMAT), Cádiz 11510, Spain
[e] IMDEA Nanoscience, Faraday 9, Madrid 28049, Spain

ARTICLE INFO

Keywords:
Microwave synthesis
Magnetic nanoparticles
Glycine
Iron oxides
Theranostics

ABSTRACT

In this study, we present a rapid method for synthesizing iron oxide nanoparticles using a microwave-assisted Schikorr reaction. We propose the use of glycine to inhibit the formation of parasitic phases even from the initial mixture of reagents. In addition to forming the nanoparticles, the method allows for the preparation of their surface for subsequent bioconjugation using a combined glucose-fructose and glycine coating at moderately low temperatures. We demonstrate that the fast formation of iron glycinates prevents the appearance of unintended compounds, which is particularly useful for controlling the Schikorr reaction and avoiding premature reactions during precursor mixing. Glycine also acts as a surfactant, limiting the growth of unwanted clusters and expanding the bioconjugation capabilities of the nanoparticles, favoring their application in theranostics. Finally, cell viability tests at different nanoparticle concentrations do not reveal significant cytotoxicity, strengthening the evidence for biocompatibility.

1. Introduction

Microwave synthesis (MWS) methods experienced considerable growth since mid-2000s for preparing a wide range of nanostructures [1–5], likely driven by the increased availability of commercial compact equipment. The repeatability and scalability possibilities that MWS offers—in many cases also entailing lower temperatures and reaction times [6]—have been especially appreciated in the production of biocompatible iron oxide nanoparticles (IONPs) for biomedical applications under Good Manufacturing Practices (GMP) conditions towards their regulatory approval, given the strict requirements set in the relevant regulations [7]. For this reason, a wide range of IONPs obtained through MWS, is also available for both in vitro and in vivo work, covering applications ranging from magnetic resonance imaging (MRI) to magnetic hyperthermia, or their combination in theranostics [8]. The more critical parameters of MWS of IONPs have been identified and studied [9–12], comparing performances with other well-established methods like thermal decomposition in high-boiling-point solvents [13], giving rise to protocols that enable faster production and that, in principle, can be extended to virtually any kind of metal oxide [14]. Methods to turn IONPs biocompatible are abundant in the scientific literature [15–19], ranging from the simplest strategies, which seek to reduce the toxicity of IONPs as much as possible, to the most complex ones, which also provide multiple functionalities [20]. The particular strategy to be followed depends on many factors, both intrinsic to the particle—composition [21], size [22] and shape [23]—and extrinsic to it—target tissue [24], internalization pathway [25], or intended circulation time [26], to name but a few. However, bringing both MWS and bio-compatibilization strategies efficiently into a single protocol continues to pose significant challenges.

Among all the iron oxide synthesis reactions described in the literature, the Schikorr reaction (Eq. 1) [27] is noted for yielding high purity

* Corresponding author at: Condensed Matter Physics department, Faculty of Sciences, Campus Universitario de Puerto Real, Puerto Real, Cádiz 11510, Spain.
E-mail address: daniel.ortega@uca.es (D. Ortega).
[1] These authors contributed equally to this work.

https://doi.org/10.1016/j.jallcom.2025.181720
Received 11 April 2025; Received in revised form 11 June 2025; Accepted 18 June 2025
Available online 19 June 2025
0925-8388/© 2025 The Author(s). Published by Elsevier B.V. This is an open access article under the CC BY license (http://creativecommons.org/licenses/by/4.0/).

magnetite (Fe_3O_4) available [28]. This reaction involves the decomposition of ferrous hydroxide ($Fe(OH)_2$) into magnetite and hydrogen gas:

$$3Fe(OH)_2 \rightarrow Fe_3O_4 + 2H_2O + H_2 \quad (1)$$

Fe^{2+} and Fe^{3+} cations undergo hydrolysis in aqueous media, with a prevalence of the 2+ state when low levels of dissolved oxygen are in place [29], which is the case of the conditions employed in this work:

$$Fe^{2+}(aq) + H_2O \rightarrow Fe(OH)^{+}(aq) + H^{+}(aq) \quad (2)$$

$$Fe^{3+}(aq) + 2H_2O \rightarrow Fe(OH)_2^{+}(aq) + 2H^{+}(aq) \quad (3)$$

Full decomposition of $Fe(OH)_2$ (as seen in Eq. 1) can typically be achieved in 4 h at 208 °C, demonstrating that high temperatures can accelerate the reaction, although such conditions may not be practical for widespread use [30]. Moreover, $Fe(OH)_2$ can remain stable indefinitely at temperatures up to 100 °C when oxygen is rigorously excluded, unless specific salts—such as $PtCl_2$ or $NiCl_2$—or finely divided metals-like Pt, Ni or Cu—are introduced into the reaction environment [30,31]. Perhaps the most significant limitation of this synthesis method is the long reaction times involved, which have constrained its adoption to both laboratory and industrial scale. This inefficiency demands significant time investments while delivering only modest returns. For example, hydrothermal treatments at 257 °C have been successfully employed to produce high-purity single-crystal Fe_3O_4, but this method typically requires extensive reaction times and strict temperature controls to minimize impurities from oxidants [32]. Another drawback is the limited control over the final product, as it often results in a phase mixture, requiring additional post-processing for separation.

Recent studies have sought to address these challenges by optimizing reaction times within the framework of the Schikorr reaction. For instance, one study reported a synthesis of ultrathin magnetic iron oxide nanoplates that achieved significant results in just one hour. This modified Schikorr reaction enhanced the formation of nanoplates, effectively reducing synthesis time while maintaining high purity [33]. Another investigation focused on a hydrothermal synthesis method that produced IONPs with tunable magnetic properties in a reaction time of approximately two hours [34]. By carefully adjusting the reaction parameters, including temperature and precursor concentration, the researchers were able to manipulate particle size and magnetic characteristics, thus improving the overall efficiency of the synthesis process (see Table S1 the Electronic Supplementary Information (ESI)).

In the present work we propose an optimized MWS approach for reducing the reaction time of the Schikorr reaction, achieving the synthesis of biocompatible Fe_3O_4 IONPs within just 10 min. Of particular note is that it entails the use of glycine to modify the reaction kinetics and sucrose to provide stabilization. The whole process integrates synthesis, biocompatibilization, and functionalization for MWS in an aqueous medium. The strategy is inspired by the structure of biological surfaces found in viruses, bacteria, and human cells, which are primarily composed of proteins and glycolipids. By employing an amino acid and a disaccharide, we mimic these natural surfaces to enhance the biocompatibility and functionality of the nanoparticles [35]. These carbohydrates are not only structural but also functional, having a distinctive role in processes like enabling or inhibiting cell recognition [36]. Amino acids and saccharides have been used as stabilizing or functionalization agents in several IONPs synthesis protocols, like thermal decomposition or co-precipitation [37–41]. However, unlike the latter, depending on the specific MWS modality that is used, there may be some technical limitations that can have a negative impact on the preparation of biocompatible IONPs: (i) maximum reaction temperatures in MWS are not as high as those typical in thermal decomposition in high-boiling point solvents, (ii) atmosphere control is not usually straightforward, and (iii) the addition of precipitants at high temperature in a conventional microwave reactor is not possible, or very limited at best. To avoid these limitations, our proposal involves employing mild reaction temperatures, an inert atmosphere, and simple initial addition of reagents. Additionally, it sets the Schikorr reaction as the basis for the MWS of IONPs, since this reaction occurs under anaerobic conditions at low temperatures [27].

The multiple advantages of the proposed method are given both by the reaction setup and the reagents used. On the one hand, MWS features high reproducibility, good scalability prospects, control over reaction start, short reaction times, a wide range of solvent choices, as well as easy operation. On the other hand, both coating reagents are low cost and provide resemblance to biological envelopes; moreover, glycine prevents Fe from reacting early before the reaction itself begins, and shows a phase-director effect towards Fe_3O_4, while sucrose becomes reductive only at moderately high temperatures. We show the director effect of glycinates and sucrose on the final iron oxide phase, also providing evidence about the biocompatibility of the resulting IONPs.

2. Experimental

2.1. Synthesis

$FeCl_2{\cdot}4\,H_2O$ (99.5 %, Thermo Scientific), NaOH (100 %, Panreac Química S.A), Milli-Q H_2O, glycine (99 %, Acros Organics), sucrose (99,7 %, Acros Organics) were used as received without further purification. Type I water was used throughout. In a typical synthesis, a 30 mL microwave glass vessel was filled with the corresponding amount of the precursor salt, glycine as ligand, and finally selected quantities of sucrose and NaOH. It is important to note that NaOH—and sucrose whenever used—was added at the last step after complexing Fe with glycine before the IONPs synthesis starts to avoid premature Fe precipitation. The formation of early iron glycinate complexes is achieved by pre-heating the mixture of glycine and Fe precursors at 65 °C for two minutes, as schematically shown in Figure S1 in the ESI.

Reagents and quantities for each reaction are given in Table 1, where all the quantities are reported per mol of Fe. Samples were labeled following a code in the form GxNy, where x and y are the molar ratios of glycine and NaOH referred to Fe^{2+}. When sucrose was added to the mixture, an extended code GxNySz was used in order to indicate the sucrose molar ratio, *z*.

To obtain an inert atmosphere and hence anaerobic conditions, the

Table 1
Compilation of reaction conditions for the whole sample set synthesized in this work. All samples involve 1 mmol Fe^{2+}.

Sample	Glycine (mmol)	NaOH (mmol)	Sucrose (mmol)
G2N6S2	2	6	2
G2N1S2	2	1	2
G1N0.25	1	0.25	0
G1N0.375	1	0.375	0
G0N0.5	0	0.5	0
G1N0	1	0	0
G1N0.5	1	0.5	0
G2N0.5	2	0.5	0
G3N0.5	3	0.5	0
G0N0.75	0	0.75	0
G0.5N0.75	0.5	0.75	0
G1N0.75	1	0.75	0
G1.5N0.75	1.5	0.75	0
G2N0.75	2	0.75	0
G2.5N0.75	2.5	0.75	0
G3N0.75	3	0.75	0
G0N3	0	3	0
G1N3	1	3	0
G2N3	2	3	0
G3N3	3	3	0
G1N3S0.3	1	3	0.3
G2N3S1	2	3	1
G3N3S2	3	3	2
G2N0.1	2	0.1	0
G0N2S2	0	2	2

air was purged out of the microwave vessels prior to the reactions by performing three N_2 bubbling cycles through a fine cannula connected to a vacuum pump. Finally, the vial was left under vacuum (10^{-3} atm, approx.). All the syntheses were carried out in a Monowave 400 microwave reactor from Anton Paar in 20 mL of type I water (with a resistivity of $\leq$ 18.2 MΩ·cm at 25 °C) under magnetic stirring at 600 rpm. The power of the microwave reactor was set to 300 W, and the heating ramp was chosen to reach 160 °C as fast as possible, remaining at this temperature for 10 min and followed by a cooling step down to 55 °C (Fig. 1). Upon completion, the so-obtained IONPs were first separated by centrifugation to eliminate most of the waste and then, separated magnetically washing them three times with type I water until a stable colloid was obtained.

2.2. Characterization

2.2.1. UV–V is spectroscopy

Samples were measured at room temperature with a Perkin Elmer Lambda 19 spectrophotometer using high precision quartz cuvettes with 10 mm path.

The measurements were performed in the 200–800 nm spectral range at a scanning rate of 240 nm/min. Samples were prepared by dissolving adequate amounts of glycine to a 0.02 M Fe^{2+} solution in type I water for the formation of Fe monoglycinate ($[Fe(GlyO)]^+$), bisglycinate ($[Fe(GlyO)_2]$), and trisglycinate ($[Fe(GlyO)_3]^-$) complexes. The resulting solutions were subsequently heated in the microwave reactor up to 65 °C for increasing time intervals to promote the formation of Fe^{2+} glycinates. Finally, the UV–VIS spectra of the solution at room temperature were registered. The formation of the three complexes is followed by the Fe^{2+} absorbance at 302 nm at room temperature. Since the formation of IONPs always takes place with either Fe^{2+} or Fe^{3+} precursors in the conditions described in the introduction (Eqs. 2 and 3), the overall process can be represented by the Schikorr reaction (Eq. 1). Initially, $FeCl_2$ samples were analyzed in the absence of glycine. As anticipated, upon the addition of NaOH, the formation of green rust was readily noticed by the color change of the medium. The underlying chemical reaction is as follows:

$$FeCl_2 + 2NaOH \rightarrow Fe(OH)_2 + 2NaCl \quad (4)$$

However, the formation of green rust is prevented by the presence of aqueous glycinate complexes. Initially, there is an electrostatic interaction between carboxylates from glycine and hydrated Fe^{2+} cations in the form of $[Fe(H_2O)_6]^{2+}$, followed by a progressive ligand exchange between these species: both oxygen from the carboxylate group of glycine and nitrogen from the amino- side coordinate with the same Fe^{2+}, displacing water molecules and eventually giving rise to the different complexes. Increasing Gly:Fe ratios of 1:1, 2:1 and 3:1 were used to promote the formation of $[Fe(GlyO)]^+$, $[Fe(GlyO)_2]$ and $[Fe(GlyO)_3]^-$. The kinetics and the formation mechanisms of these complexes have been reported by K. Micskei et al. Further, relevant literature provides evidence on the formation of progressively more complex Fe(II) glycinates as the Fe(II) to glycine molar ratio is increased, as attested by mass spectrometry [42], paramagnetic relaxation [43], voltammetry [44], or electromotive force measurements at different pHs [45].

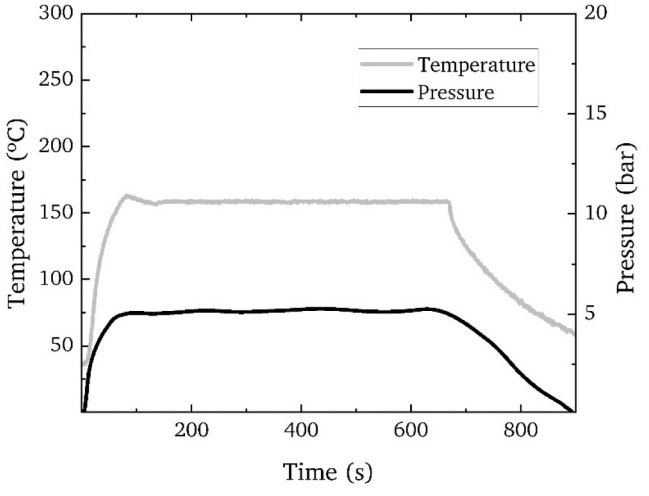

Fig. 1. Typical temperature and pressure profiles over time during the synthesis of the set of samples analyzed in this study.

In this work we have assessed the occurrence of the $[Fe(GlyO)]^+$, $[Fe(GlyO)_2]$ and $[Fe(GlyO)_3]^-$ complexes through UV/Vis spectroscopy by taking advantage of the onset of ligand to metal charge transfer (LMCT) bands with increasing glycine concentrations. The corresponding spectra of the three complexes were recorded after microwave preheating, and compared with that of an Fe^{2+} solution of the same concentration (0.02 M) (Figure S2, ESI). First, we follow the evolution of the Fe^{2+} absorbance peak at 302 nm at room temperature to increase MW heating times at 65°C for two minutes. The results (Figure S2, ESI)† indicate, first, the enhancement of this electronic transition when glycine is introduced into the medium, suggesting that the formation of complexes is effective. Secondly, we set two minutes as the microwave heating time considering the observed evolution of the absorbance at 302 nm (Figure S2, ESI).

2.2.2. X-ray diffraction (XRD)

The diffraction profiles were obtained with a Rigaku Smartlab diffractometer, using Cu $K\alpha_1$ [Å] = 1.54060, $K\alpha_2$ [Å] = 1.54443, and Kα [Å] = 1.39225. The samples were magnetically separated and dried with a N_2 flux in an XRD glass sample holder. Non-magnetic samples were prepared by centrifuging the sample at 10.000 rpm and allowing them to dry in a glass sample holder for XRD measurements. The scattering from the samples was measured from 5° to 100° with a step size of 0.0264 2θ and a scan time of 1 s. Lattice parameters (a) were estimated from the Rietveld refinement of the corresponding experimental diffraction profiles using the software X´Pert High- Score Plus from Malvern Panalytical [46].

2.2.3. Fourier-transform infrared spectroscopy (FTIR)

FTIR was used to obtain information regarding the bonding between the capping agents and the IONPs surface. The experiments were recorded with a Bruker Alpha System Spectrophotometer using the KBr wafer technique with the same quantity of sample for all measurements. Samples were measured in dried form after centrifugation, mixed with the relevant amount of KBr and then pressed into a thin wafer. The measurement was the mean of 64 scans with a resolution of 2 cm^{-1} between 4000 cm^{-1} and 400 cm^{-1} at room temperature. A baseline correction was applied, and the corresponding band assignment was carried out mainly using the NIST database [47].

2.2.4. Raman spectroscopy

Raman Spectroscopy was carried out in a Senterra Raman Spectrometer confocal (Bruker Optic, Ettlingen, Germany) with a 3–5 cm^{-1} resolution. The measuring parameters were the following: 785 nm laser excitation at 1 mW, 3 s scanning, 4 co-additions, and an objective numerical aperture of 0.75. Samples were prepared by depositing a few milligrams of IONPs onto a cover glass under a N_2 flow. The standard measurements implied 3–5 cm^{-1} scanning areas of the samples, obtaining an average spectrum from 12 selected points. The software Opus from Bruker was used to subtract the background. The spectra are the average of 12 measurements at different points of the sample.

2.2.5. Vibrating sample magnetometry (VSM)

Room temperature hysteresis loops were measured using a 7410 Lake Shore vibrating sample magnetometer. Samples were dried and

weighed for measurement; more specifically, 10 mg of IONPs were measured and then encapsulated in gelatin capsules, pressed with cotton wool, and finally loaded into the sample holder. Measurements were carried out from zero to a maximum applied field $\mu_0 H = 5$ T. Specific magnetization (σ_S) data were extracted using a nonlinear fit to Langevin equation [48]:

$$\sigma(H) = \sigma_S \bullet (\coth(z) - 1/z) \quad (5)$$

where σ_S is the saturation magnetization, H the intensity of the externally applied magnetic field, and z is $\mu_0 mH/(k_B T)$, being m the magnetic moment of the nanoparticles, $\mu 0$ the magnetic permeability of free space, k_B the Boltzmann constant, and T the temperature.

2.2.6. Transmission electron microscopy (TEM)

Samples were 10x diluted in MilliQ water and then sonicated before imaging. To collect a representative number of IONPs, a thin layer of continuous carbon grid was briefly immersed into each colloid and subsequently let dry under a glass cover to avoid sample contamination. Conventional and high-resolution transmission electron microscopy (TEM/HRTEM) were acquired using a FEI TALOS F200X electron microscope operating at 200 kV. Digital diffraction patterns (DDP) obtained from experimental HRTEM images correspond to the log-scaled power spectrum of the Fourier transform of the intensity distribution in the images. These DDP allow measuring the associated lattice fringe spacings and angles by pointing the intensity maximum in the diffraction spots. HRTEM image processing and phase identification were performed using the DigitalMicrograph© software from Gatan together with the EjeZ program developed by Pérez-Omil et al.[49]

2.3. Cell viability assays

2.3.1. Choice of cell cultures

The EO771 murine breast cancer cell line and the Eahy926 human endothelial hybrid cell line were selected to evaluate the cytotoxicity and biocompatibility of glycine- and sucrose-coated IONPs due to their relevance in modeling tumor and vascular biology, respectively. EO771 cells represent an immunocompetent, triple-negative breast cancer model derived from C57BL/6 mice, making them highly suitable for studying nanoparticle interactions in preclinical cancer research, especially in syngeneic murine models where immune interactions are preserved [50]. Their aggressive phenotype and high metabolic activity provide an ideal platform to assess nanoparticle uptake, cytotoxicity, and therapeutic potential in a tumor-like environment [51]. In contrast, Eahy926 cells, derived from the fusion of human umbilical vein endothelial cells (HUVECs) with the A549 lung carcinoma cell line, retain key features of vascular endothelial cells such as tight junction formation, angiogenic signaling, and vascular permeability [52]. Their use allows for the evaluation of nanoparticle safety in non-cancerous but highly responsive vascular cells, which are among the first to encounter systemically delivered nanomaterials [53]. Together, these two cell lines offer a comparative model that captures both the pathological (tumoral) and physiological (vascular) contexts, enabling a more comprehensive assessment of nanoparticle biocompatibility and potential off-target effect.

2.3.2. Assays and data analysis

Prior to these assays, selected nanoparticle suspensions were sterilized by filtration (0.22 μm) prior to use in cell culture experiments. EO771 murine breast cancer cells and Eahy926 human endothelial hybrid cells were cultured in complete Dulbecco's Modified Eagle Medium (DMEM) supplemented with 10 % fetal bovine serum (FBS) and 1 % penicillin-streptomycin, under standard conditions (37 °C, 5 % CO_2, humidified atmosphere). Cells were maintained in T-75 flasks and subcultured at 70–80 % confluence using 0.25 % trypsin-EDTA. Cells were seeded into 96-well plates at a density of approximately 5000 cells per well and allowed to adhere for 24 h. After attachment, cells were treated with glycine- and sucrose-coated IONPs at varying concentrations (10, 50, 75, 100, and 250 μg/mL) for 24 h. Control wells were treated with nanoparticle-free medium. Cell viability following nanoparticle exposure was assessed using the Alamar Blue assay, a resazurin-based metabolic indicator of cell health. After 24 h of treatment, the medium was removed and replaced with fresh medium containing 10 % Alamar Blue reagent (v/v). Plates were incubated at 37 °C for 2–4 h, after which fluorescence was measured using a microplate reader at excitation/emission wavelengths of 560/590 nm. Viability was expressed as a percentage relative to untreated control cells. All experiments were performed in triplicate (n = 3 independent replicates). Data are presented as mean ± standard deviation. Viability values were analyzed using one-way ANOVA followed by post hoc Tukey's test to assess statistical significance between treatment groups, with $p < 0.05$ considered significant.

3. Results and discussion

In Fig. 2 we compare the spectral evolution of the extinction coefficient of the three complexes and Fe^{2+} solutions after a two-minute microwave heating. It can be noticed that, in addition to the aforementioned peak at 302 nm (33113 cm^{-1} in Fig. 2), there are other lower energy features differentiating between the resulting complexes and the initial Fe^{2+} solution. Charge transfer bands are usually broad, and display high extinction coefficients [54], typically $\geq$ 50000 M^{-1} cm^{-1}, which is the case of those observed in Fig. 2 from approximately 32000 cm^{-1} onwards. The aqueous Fe^{2+} solution exhibits the lowest extinction coefficients due to more modest ligand interactions with water molecules primarily involving weak d-d transitions, such as the spin-allowed quintet $^5E(D)$ (appearing typically at around 10500 cm^{-1}) [55]. As glycinate ligands with N and O electron-donating atoms are introduced, beginning with $[Fe(GlyO)]^+$, extinction coefficients are enhanced, suggesting the onset of more defined ligand field effects and charge transfer transitions. As predicted by the Tanabe-Sugano diagrams for a high-spin d^6 system in an octahedral field like that of Fe^{2+}, the observed spectral enhancements are attributed to the initial LMCT facilitated by the glycinate coordinating with the Fe^{2+} center, enriching the electronic interactions. In a general fashion, progressing to the formation of more complex glycinates, each stepwise increase in ligand coordination not only strengthens the ligand field but also the LMCT transitions. Finally, two crossovers can be observed between [Fe

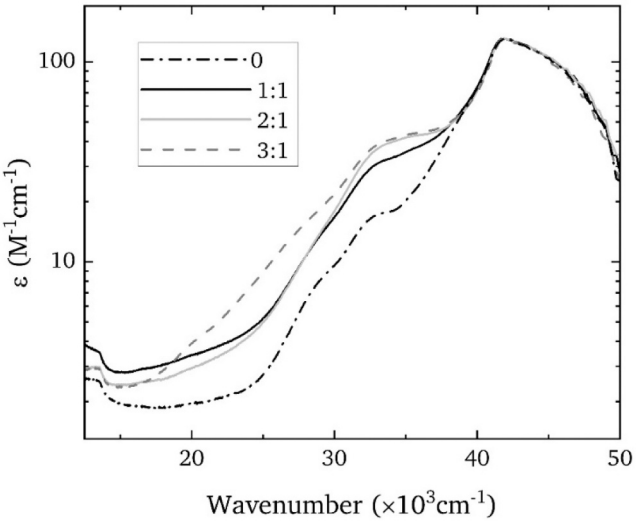

Fig. 2. Molar extinction coefficient spectra of an Fe^{2+} aqueous solution and glycinate complexes formed with different Gly/Fe^{2+} molar ratio indicated in the legend after 2 min MW heating time.

$(GlyO)]^+$ and $[Fe(GlyO)_2]$ spectra at ca. 27500 cm^{-1} and then between $[Fe(GlyO)]^+$ and $[Fe(GlyO)_3]^-$ ones, both due to the higher prevalence of d-d interactions towards lower wavenumbers.

Fig. 3 presents the room-temperature XRD profiles of three representative samples from the set of compositions listed in Table 1, illustrating the primary distributions of crystalline phases observed. These were α-Fe_2O_3 (Fig. 3a) with a = 5.035 Å, γ-Fe_2O_3 (Fig. 3b) with a = 8.336 Å, and Fe_3O_4 (Fig. 3c) with a = 8.397 Å. The shorter reaction times resulting from the increase in reaction temperature (160 °C) also lead to the agglomeration of the IONPs, as it has been observed in the synthesis of other nanoparticles [28] and nanoplates [33,56].

The influence of the NaOH/Fe ratio on the crystallinity of IONPs was studied by XRD on a set of samples with a constant 2:1 Gly:Fe ratio (Fig. 4). After the addition of the iron chlorides to the aqueous solution, the pH decreases by a certain amount due to the dissociation of the salt and the formation of hydroxoaqua Fe(II) complexes (Eqs. 2–3) [55]. These hydroxoaqua Fe(II) complexes are more stable at low pH. Upon increasing the pH by adding a base in the absence of glycine, a precipitate forms. However, when glycine is present, no precipitate is observed, due to the enhanced solubility of Fe(II) glycinates at higher pH levels in aqueous media [56]. Using Fe^{2+} as the precursor predominantly leads to the formation of Fe_3O_4, which can be attributed to the partial oxidation of Fe^{2+} via the Schikorr reaction (Eq. 1) as is the case for sample G2N3S1. The added NaOH stabilizes the precursor $Fe(OH)_2$ in the Schikorr reaction and shifts the equilibrium towards the products (see Eq. 1), i.e. towards Fe_3O_4. Notably, increasing the NaOH concentration while keeping precursor concentration constant led to a significant increase in crystallite size, from 16.40 ± 1.42 nm in sample G2N3S2 to 108.72 ± 15.79 nm in sample G2N6S2 (see Table S3, ESI). This growth is related to the promotion of the Schikorr reaction.

The presence of glycinates acts as an inhibitor, preventing the formation of hydroxides at low temperature. The dissociation and nature of the precursor salts may nevertheless influence the reaction pathway towards iron oxide formation, as they partially dictate the rate at which the solution and any intermediate phases reach pH equilibrium [41]. This temperature-controlled approach is crucial for the preferential formation of the Fe_3O_4 phase in microwave reactors. Accordingly, the NaOH concentration influences both the resulting crystallite phase and sizes. When larger NaOH/Fe ratios are used (see Fig. 4a, b and c), the

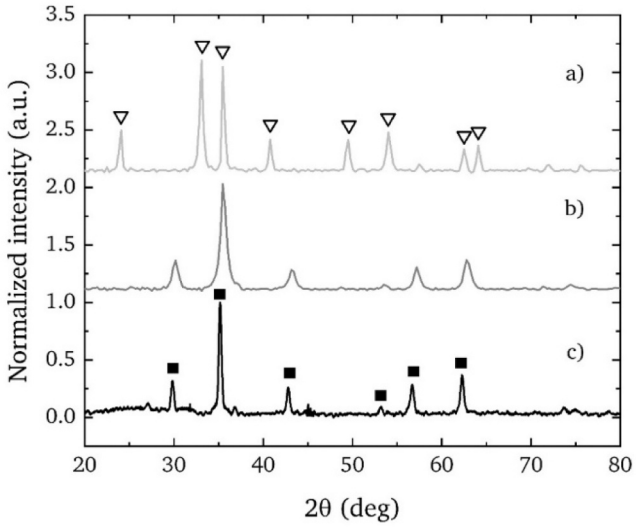

Fig. 3. Room temperature XRD profiles of samples (a) G1N0, (b) G1N0.375, and (c) G2N3S1. The most relevant crystallographic planes have been indexed using the corresponding PDF Cards 01–071–4918 for Fe_3O_4, 01–025–1402 for γ-Fe_2O_3 and 01–001–1053 for α-Fe_2O_3. The corresponding indexation of α-Fe_2O_3 and γ-Fe_2O_3/Fe_3O_4 peaks is represented by open triangles and full squares, respectively.

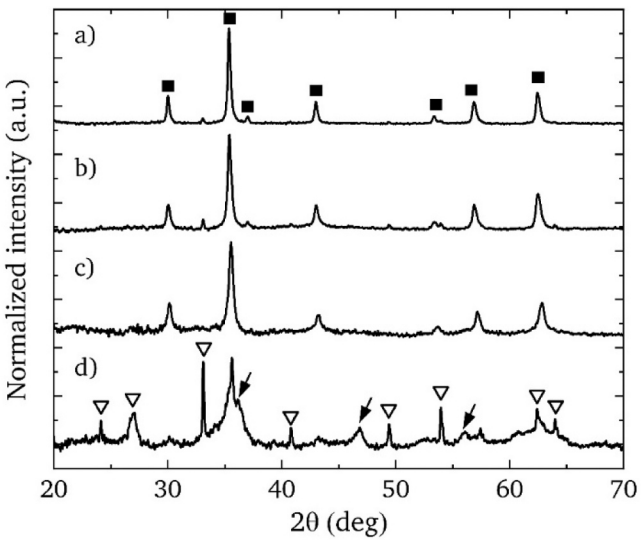

Fig. 4. Room temperature XRD profiles of samples with a constant (2:1) Gly:Fe ratio and increasing NaOH:Fe ratios. a) G2N0.1, b) G2N0.5, c) G2N0.75 and d) G2N3. The corresponding indexation of α-FeOOH, α-Fe_2O_3 and γ-Fe_2O_3/Fe_3O_4 peaks is represented by arrows, open triangles and full squares, respectively.

corresponding profiles only exhibit the characteristic Fe_3O_4 peaks with a narrower width and a progressively lower background noise. This phenomenon is attributed to the enhanced nucleation and growth processes facilitated by the NaOH excess. Furthermore, the Rietveld refinement of the XRD profiles revealed a certain increase of the crystal size with increasing NaOH/Fe ratios (Table S3, ESI). This trend aligns with the observed shift towards sharper and narrower diffraction peaks associated with higher NaOH/Fe ratios. It is noteworthy that a NaOH/Fe ratio below 0.375 leads to an incomplete reaction, as evidenced in Fig. 4d, resulting in a noisier diffraction profile and the formation of undesirable by-products alongside the targeted phase. A low NaOH/Fe^{2+} ratio promotes an increased oxidation of Fe^{2+} to Fe^{3+}, which favors the crystallization of α-Fe_2O_3 such as sample G1N (Fig. 4d). This behavior is consistent with the use of Fe^{3+}, where only α-Fe_2O_3 crystallizes (Fig. 4b).

The crystallite size and lattice parameter *a* were studied as a function of the Gly:Fe ratio (as detailed in the ESI), with the bisglycinate pathway producing a value closely aligned with Fe_3O_4, indicating greater structural similarity and suggesting improved crystalline coherence and phase purity. We hypothesize that this is due to complete charge compensation, preventing non-specific interactions and stabilizing the complex against temperature increases, as inferred from the following experimental observations.

IONPs were able to nucleate and grow without any surfactant, indicating that the reaction was driven primarily by the precipitant. When no glycine was present, the reaction initiated immediately upon mixing the reagents before heating, resulting in large agglomerates of IONPs (e.g., samples G0N0, G0N0.5, G0N0.75, and G0N3, Table S3, ESI). In contrast, in the presence of glycine, the initially formed iron glycinates reacted at higher temperatures, preventing the formation of large agglomerates. Higher glycine concentrations, however, typically led to a reduction in crystallite size while a remained unchanged, suggesting that glycine complexation inhibited crystallite growth, leading to smaller particles. When sucrose was introduced for dual coating with glucose and fructose, the experimental lattice parameter a that most closely matched the theoretical value of Fe_3O_4 (a = 8.402 Å) was achieved at a relative molar ratio of glycine:sucrose:Fe^{2+} = 2:1:1. Additionally, increasing sucrose concentration resulted in a further reduction in crystallite size, as shown by the Rietveld analysis results (Table S3, ESI).†

To corroborate XRD measurements, we have carried out Raman spectroscopy of three representative IONPs samples (Fig. 5). Raman

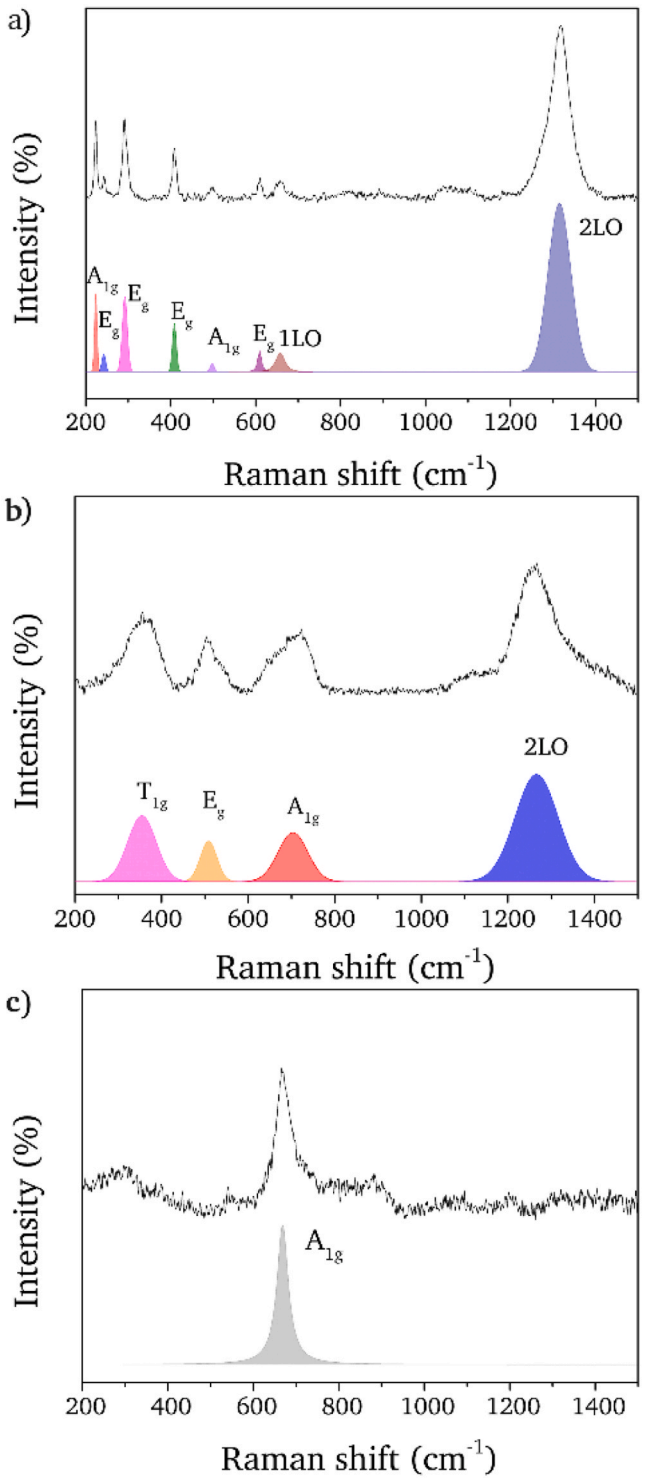

Fig. 5. Room temperature Raman spectra of samples G1N0 (a), G1N0.375 (b) y G2N3S1 (c).

active phonons of the different iron oxide phases and assignments of the observed wavenumbers are listed in Table 2. For those samples in which α-Fe_2O_3 is found, all the Raman-active modes are present in the spectrum. Those modes that arise from the Γ point (the center of the Brillouin zone), are the external phonons (E_g modes), the symmetric stretch or bend band for centrosymmetric molecules ($A_{1\,g}$ modes), and the 1LO and the 2LO, which are related to two-phonon scattering process [57]. In the case of samples containing Fe_3O_4, Raman active modes are $A_{1\,g}$(R), E_g(R), and T1(R), which refers to the torsional vibration of a molecule

Table 2
Assignment of phonon frequencies of different Raman vibrational modes observed in Fig. 5.

Compound	Wavenumber (cm^{-1})	Assignment
α-Fe_2O_3 (Sample G1N0)	224, 500	$A_{1\,g}$
	244, 290, 409, 610	E_g
	657	1LO
	1317	2LO
γ-Fe_2O_3 (Sample G1N0.375)	722	$A_{1\,g}$
	508	E_g
	375	$T_{1\,g}$
	1264	2LO
Fe_3O_4 (Sample G2N3S1)	677	$A_{1\,g}$

involving rotation around an axis passing through two atoms [57,58]. Finally, the more complex unit cell of γ-Fe_2O_3 results in Raman active phonons T_1, E and A_1 modes are $A_{1\,g}$(R), E_g(R), and T_1(R), which refers to the torsional vibration of a molecule involving rotation around an axis passing through two atoms [57,58]. Finally, the more complex unit cell of γ-Fe_2O_3 results in Raman active phonons (356, 493 and 695 cm^{-1}) which depend on the sample preparation method [58]. Additionally, it has been reported that bands assigned to 1LO and 2LO modes (660 and 1320 cm^{-1}, approximately), experience a strong intensity enhancement in the Raman spectra collected from the nanoparticles, caused by two longitudinal optical phonons (LO) near the band gap [59]. The Raman phonon modes observed in the spectrum of sample G1N0 confirm exclusively the presence of the α-Fe_2O_3 phase, as evidenced by the absence of additional Raman phonons modes (Fig. 5a). Fig. 5b of sample G1N0.375 exhibits all the characteristic phonons of the cubic spinel phase γ-Fe_2O_3. Conversely, the spectrum of sample G2N3S1 (Fig. 5c) presents a poor signal to noise ratio and the only mode clearly visible is the A_{1g}(R) one associated with Fe_3O_4, although two T_{2g} modes at 296 cm^{-1} and 581 cm^{-1} can be guessed. These observations are in line with the XRD data analysis where α-Fe_2O_3 was assigned to sample G1N0 and γ-Fe_2O_3 to sample G2N3S1.

Exploring the persistence of the coating compounds (glucose, fructose, and glycine) in the magnetic nanoparticles surface after washing cycles is crucial for their various applications. For this purpose, FTIR spectra were acquired for the entire set of samples at room temperature after they were subjected to a minimum of three washing cycles. Fig. 6 displays the FTIR spectrum of sample G2N3S1, as representative of those in Table 1 synthesized with sucrose, indicating the position of the main bands whose nominal assignments are collected in Table 3. Note that this spectrum is shown as representative of the whole set, as the other samples feature the same bands without noticeable changes.

The presence of glycine is usually evidenced by bands like the $\nu_{N\text{-}H}$ one from the amino- end of glycine should be located in the 3300–3500 cm^{-1} region; however, this band cannot be unambiguously recognized given the intense absorption in that wavenumber range, where it partially overlaps with the set of $\nu_{O\text{-}H}$ bands from glucose and fructose molecules within 3200–3600 cm^{-1} (typically 3392, 3296, and 3243 cm^{-1} for glucose, and 3520, 3396 cm^{-1} for fructose) [60], which are usually more visible and broader due to the typical formation of intermolecular hydrogen bonds. Since sample colloids are stored at pH = 7.2, glycine is above its isoelectric point (≈ 6) and thus in its zwitterionic form with protonated amino- ends. The latter will bind to the negatively charged FeO- groups at the IONPs surface through a hydrogen bond, hence producing a weakening of the surface-bonded N-H with respect to that of the non-bonded N – H and producing a shift towards lower wavenumbers. The shoulder at 3250 cm^{-1} may well reflect this aspect.

Other distinctive bands of glycine are featured in Fig. 6 within the 1660–1550 cm^{-1} range, more specifically the $\delta_{N\text{-}H}$ and the $\nu_{C=O-Fe-O}$, which are slightly shifted due to the implicit bonds with the surface of

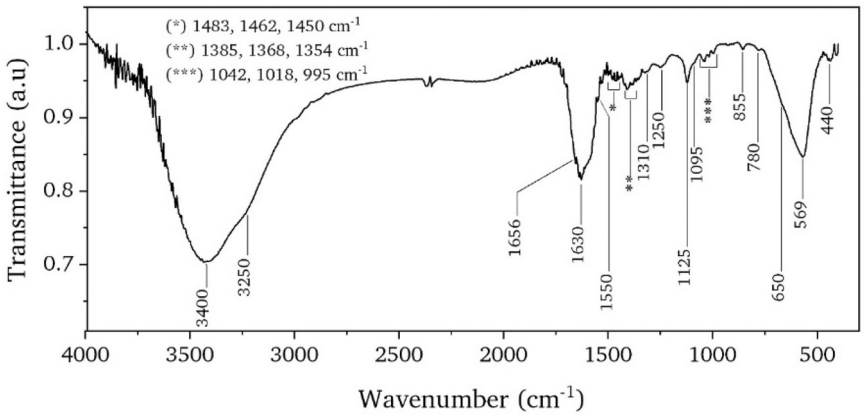

Fig. 6. Room temperature FTIR spectrum of sample G2N3S1.

Table 3
Assignment of the different vibration modes present in the room temperature FTIR spectrum of sample G2N3S1. Key: ν - stretching, δ_{ip} - bending, δ_{sci} - scissoring, ω - wagging, τ - twisting, *asym* – asymmetric, *sym* – symmetric, *ip* – in plane.

Wavenumber (cm^{-1})	Mode assigned	Compound
3400	$\nu_{O\text{-}H}$	glucose, fructose
3250 (shoulder)	$\nu_{N\text{-}H}$	glycine
1656 1630 1550	$\delta_{N\text{-}H,\ ip}$ $\nu_{C=O\text{-}Fe\text{-}O}$	glycine
1483 1462 1450	$\delta_{CH2,sci}$	glucose, fructose
1385 1368 1354	ω_{CH2}	glucose, fructose
1310	$\delta_{C\text{-}CH,ip}$, $\delta_{O\text{-}CH,ip}$	glucose, fructose
1250	$\delta_{O\text{-}H,ip}$	glucose, fructose
	$\nu_{C\text{-}N}$	glycine
1125	$\nu_{C\text{-}O\text{-}C}$	pyranose and furanose from glucose and fructose
	$\nu_{C\text{-}O}$	glucose and fructose
1095 1042 1018	$\nu_{C\text{-}O}$, $\nu_{C\text{-}O\text{-}C}$, $\nu_{COH,ip}$	glucose and fructose
995	$\delta_{CCH,ip}$, $\delta_{CCO,ip}$	
855	$\delta_{C\text{-}CH}$, $\nu_{C\text{-}O}$, $\nu_{\text{-}O}$, $\nu_{pyranose}$	glucose
	$\delta_{C\text{-}H}$, $\nu_{C\text{-}C}$, $\delta_{C\text{-}CH}$	fructose
	$\nu_{C\text{-}N,\ sym}$	glycine
780	$\delta_{C\text{-}CO}$, $\delta_{C\text{-}CH}$	glucose and fructose
650	$\delta_{CO\text{-}O}$	glycine
569	$\nu_{Fe\text{-}O\ (Td}$	nanoparticles
440	$\nu_{Fe\text{-}O\ (Oh)}$	nanoparticles

the nanoparticles. However, it cannot be discarded that the $\nu_{C=O}$ of fructose and $\nu_{CH=O}$ of glucose, expected at around 1700 cm^{-1}, also contributes here due to the fact that both molecules are not in a free form but bonded to the surface of the nanoparticles [61]. In addition, the $\nu_{C\text{-}N}$ from glycine overlaps at 1125 cm^{-1} with the ν_{C-O} band from glucose and fructose, as well as the ν_{C-O-C} band from the pyranose and furanose rings also from glucose and fructose molecules. The $\nu_{C-N,sym}$ mode of glycine —if actually present —would overlap at 855 cm^{-1} with other possible contributions like the $\nu_{C\text{-}C}$ from glucose and fructose, theoretically expected at 837 y 874 cm^{-1} [60]. A barely perceptible band at 900 cm^{-1} could be indicative of the ρ_{CH2} mode from glycine, and the δ_{CO-O} mode from the carboxylate moiety of glycine is present as a shoulder at 650 cm^{-1} at the left side of the broad absorption centered at 575 cm^{-1}.

Regarding glucose and fructose molecules, there are other distinctive bands in addition to those already discussed. Although bending modes from C—H bonds in glycine may show up within the 1300–1500 cm^{-1} range, the set of weak bands experimentally observed in this region (bending vibrations δ_{CH2} at 1483, 1462, 1450 cm^{-1}, and wagging vibrations ω_{CH2} at 1385, 1368, 1354 cm^{-1}) are assumed to come from the much longer backbones of glucose and fructose. Most of these bands show a weak blue shift towards higher wavenumbers, which indicates either the existence of hydrogen bonds between adjacent saccharide molecules or slight conformational changes in the latter due to the formation of bonds between these molecules and the surface of the nanoparticles.

In the spectral range with the lowest wavenumbers or “fingerprint” region, the main contributions come from glycine and the nanoparticles. Whereas the main ν_{Fe-O} band from the tetrahedral sites in the spinel structure of the Fe_3O_4 nanoparticles (569 cm^{-1}) is usually broad, in our study appears broader than expected [62], which is nonetheless consistent with the variety of moieties bonded to their surface. In addition to these considerations, the $\delta_{CO\text{-}O}$ bands from glycine [41] are contributing to that widening, manifesting itself in the form of the 650 cm^{-1} shoulder, and in a less pronounced way, at $\approx$ 500 cm^{-1}. Finally, the 400 cm^{-1} band arise from the ν_{Fe-O} at the octahedral sites of Fe_3O_4. Of note is that the intensity relation between both 569 and 440 cm^{-1} bands does not follow the numerical proportion between T_d and O_h sites in the spinel structure but the change in the magnitude of the dipole moment of the molecule during the vibration. In short, T_d modes involve coordinated displacements of oxygen atoms that produce a large net charge displacement, whereas O_h modes involve pairs of oxygen atoms moving in opposite directions that may eventually cancel out and thus small dipole change [63,64].

Fig. 7 shows the 300 K hysteresis loops of three representative samples of the whole set. Considering the different phases found in the samples, i.e., Fe_3O_4 in G2N3S1, a mixture of Fe_3O_4 and γ-Fe_2O_3 in G3N3S2, and finally γ-Fe_2O_3 in G1N0.375, there is a match between these phases and the downward trend of the experimental σ_s extracted from the corresponding loop (Table 4). However, a closer inspection reveals that these σ_s values are lower than the bulk counterparts of the corresponding phase [65]. Whereas magnetic behavior is not dominated by surface spins, since for 15–26 nm nanoparticles the fractions of surface atoms are 5 and 3.75 %, respectively, their contribution is still nonnegligible and may be reflected in the experimental measurements. These surface spins in spinel iron oxides show a certain degree of

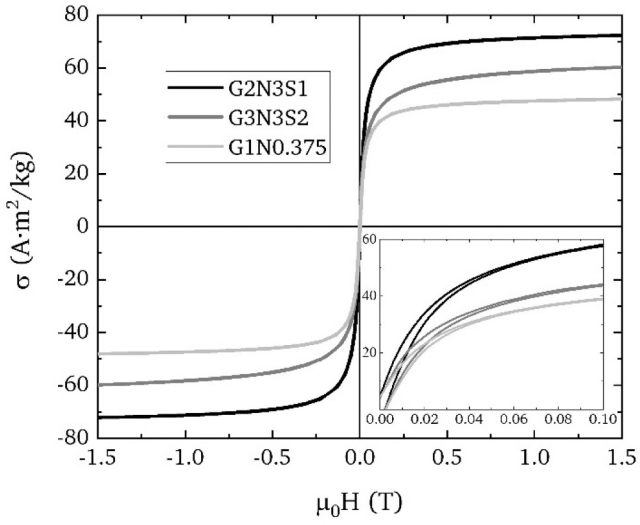

Fig. 7. Hysteresis loops at 300 K from samples G2N3S1, G3N3S2 and G1N0.375. The inset features a zoom into the low field region where $\mu_0 H_C$ can be better appreciated.

Table 4
Main magnetic parameters derived from the fit to Eq. 5 from room temperature DC magnetization measurements of samples G1N0.375, G3N3S2 and G2N3S1. Crystallite size (d) and lattice parameter (a) from the corresponding Rietveld analysis of the experimental XRD data are also indicated for reference.

Sample ID	d (nm)	a (Å)	σ_s (A·m²/kg)	$\mu_0 H_C$ (T)
G1N0.375	14.90	8.351	48.22	2.60×10^{-4}
G3N3S2	16.40	8.365	60.45	2.32×10^{-4}
G2N3S1	26.00	8.401	72.27	2.24×10^{-4}

correlated/uncorrelated disorder that results in a nonmagnetic layer [66] with changing thickness under different field intensities, as recently demonstrated [67]. The maximum thickness is typically around 1 nm, and its extent depends on many different variables, like composition, density of defects, particle size, or coating nature, among others [68]. The thickness of the nonmagnetic disordered layer of nanoparticles can be approximately estimated from the experimental σ_s values using the equation $\sigma_{s(\exp)} = \sigma_{s(bulk)} \cdot (1 - 6t/r)$ [69], where $\sigma_{s(exp)}$ is the experimental saturation magnetization, $\sigma_{S(bulk)}$ is the bulk saturation magnetization, r the particle size and t the non-magnetic disordered layer. Considering the bulk σ_s values for Fe_3O_4 (92 A·m²/kg) and γ-Fe_2O_3 (76 A·m²/kg) at 20 °C [48,65], together with the phase composition for each of the three measured samples, the obtained t for samples G2N3S1, G3N3S2 and G1N0.375, respectively, are 0.5, 0.5 and 0.8 nm. In other words, the difference between measured and bulk σ_s can be explained on this basis for those samples. Similar σ_s values have been determined by other authors in Fe_3O_4 and γ-Fe_2O_3 nanoparticles with different surface coatings [70].

In this study, TG measurements were conducted placing a magnet around the sample space so that both the magnetic force acting on the sample and the weight losses contribute to the changes in the thermogram recorded on heating. TG measurements in a magnetic field provide further information about the phase transformations taking place in the samples and their Curie temperature [71]. Beyond the direct information on weight losses associated with the evolving of the different products at distinct temperature ranges, when samples are heated under a static magnetic field, any magnetic phase transition causes an apparent weight loss and can be detected as changes in mass in the TG curves. A description of the general features of the TG without magnetic field can be found in the ESI (see Figure S5 and related text). Fig. 9 shows the TG curves of samples G2N3S1, G3N3S2, and G1N0.375 registered with an external magnetic field, where a progressive weight loss for each one comes to completion below 600 °C. In the case of sample G2N3S1, a plateau is observed within the 200–350 °C range, suggesting a significant slowdown in the rate of total weight loss. This feature derives from the interplay of three concomitant processes: (i) the loss of the organic mass from the nanoparticles surface, (ii) the weight gain due to the oxidation of initial magnetite, and (iii) the apparent weight loss that is due to a less intense interaction between the sample and the external field because of the oxidation to γ-Fe_2O_3, which features a lower magnetization than Fe_3O_4 at the applied field. In other words, whereas the expected weight loss due to the organic matter (see Figure S5 in the ESI) adds to the "magnetic" apparent loss of the magnetic transition from Fe_3O_4 → γ-Fe_2O_3, the gain of mass due to the oxidation counterbalances them. Thus, this observation and the temperature range where it is observed are with the oxidation of the initial Fe_3O_4 to γ-Fe_2O_3, which usually happens at 200 – 250 °C in crystals under 300 nm [71]. The oxidation process implies a reduction of density, a mass increase as oxygen is taken up by the IONPs, and a reduction in the number of Fe atoms per unit cell as the transformation to γ-Fe_2O_3 proceeds. A complete weight loss is obtained in the vicinity of 600 °C, where the final oxidation of γ-Fe_2O_3 to α-Fe_2O_3 takes place at slightly different temperatures for each of the samples, namely 557.4 °C for sample G2N3S2, 560 °C for sample G1N0.375, and 565.3 °C for sample G2N1S2 (inset in Fig. 8). A consecutive TG of the same sample, G3N3S2 recorded after the first TG run, shown in Fig. 9, corroborates the eventual transformation from γ-Fe_2O_3 to α-Fe_2O_3. In this second TG, the only weight loss shown in the entire temperature range is the drop at 645 °C, which is ascribable to the Néel temperature of α-Fe_2O_3, where it transforms from a canted antiferromagnet to a paramagnet. This transition has been reported to happen in a more or less broad range centered at about 682 °C [72].

Sample G2N3S2 exhibits a significant decrease in magnetic strength, as it is a mixture of phases where the oxidation of some of the IONPs (from Fe_3O_4 to γ-Fe_2O_3), along with the weight loss occurring in those regions, leads to this decline. By examining the derivative weight loss (Fig. 8, inset), we can see that all the samples show a relatively similar Curie temperature around 560 °C. This is because all samples, whether they are Fe_3O_4, γ-Fe_2O_3, or a mixture of phases, oxidize to their

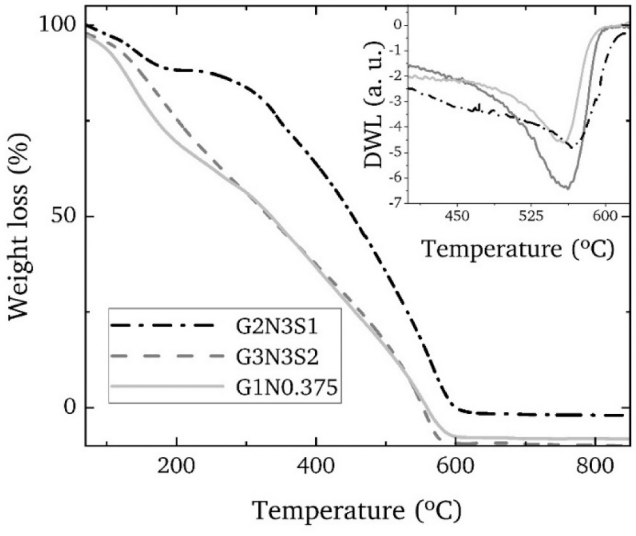

Fig. 8. TG under a static magnetic field of samples G2N3S1, G3N3S2, and G1N0.375, where the 100 % weight loss corresponds to the apparent weight of the sample due to the magnetic interaction with the applied field at 50 °C. Note that the negative weight loss values upon completing the γ-Fe_2O_3 → α-Fe_2O_3 phase transition correspond to the actual weight loss, which is superimposed to the magnetic interaction. The inset shows the DTG curves for samples G2N3S1, G3N3S2, and G1N0.375. DWL stands for derivative weight loss.

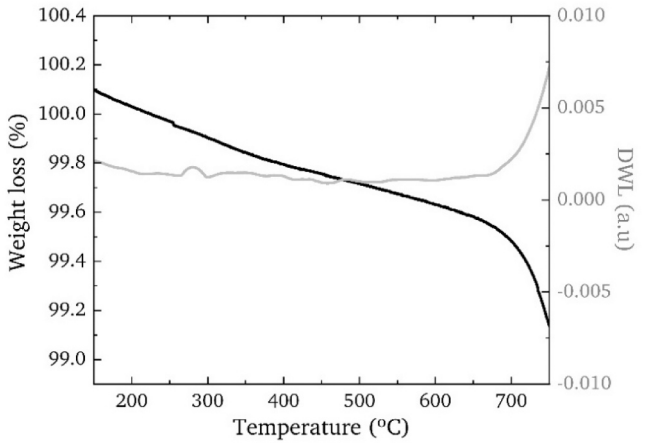

Fig. 9. Second TG curve (black line) and the corresponding DTG (light grey) for sample G2N3S1 acquired just after undergoing the first TG analysis under the same experimental conditions (10 °C/min; carrier gas: mixture of 21 % O_2 in N_2). DWL stands for derivative weight loss.

maximum state of oxidation, i.e., γ-Fe_2O_3. Once the Curie temperature of this phase is reached, a topotactic structural change occurs that is associated with the complete loss of magnetic force.

Given its composition and physical properties, sample G2N3S1 was chosen as an exemplary IONPs system for subsequent cytotoxicity tests. The analysis of the viability data for EO771 cells and Eahy926 exposed to these IONPs reveals a clear dose-dependent cytotoxic effect in both cell lines (Fig. 10). At lower concentrations (10–75 μg/mL), cell viability remains above 90 % for both EO771 and Eahy926, indicating high biocompatibility and minimal acute toxicity. Viability remains above 85 % for concentration of 100 μg/mL, which, according to the criteria established by the ISO 10993–5:2009 standard [73], is not considered indicative of a cytotoxic effect, as a 30 % decrease in viability is the threshold for cytotoxicity. However, at high concentrations (250 μg/mL), a notable decrease in viability is observed, with both cell lines showing a drop to approximately 72.5 % at 250 μg/mL. This points out that the observed cytotoxicity is not cell-type specific but rather a generalized response driven by the physicochemical properties of the IONPs. It must be noted that this high concentration value has been tested just for demonstration purposes, since cytotoxicity and uptake studies for nanoparticles usually test concentrations below 100 μg/mL—higher concentrations induce saturated nanoparticle uptake and rarely correspond with realistic clinical dosing. Glycine, as zwitterionic amino acid, contributes to colloidal stability and reduced surface charge, while both glucose and fructose from the decomposition of sucrose, acting as surfactants, enhance hydrophilicity and dispersion in aqueous media [74]. Despite these coatings, the lack of selectivity between cancerous and non-cancerous cells implies that the internalization and biological interaction of the studied IONPs are not preferential toward malignant cells, potentially due to shared uptake mechanisms such as endocytosis [75].

The observed viability trend suggests that beyond a certain concentration threshold, nanoparticle accumulation and intracellular oxidative stress may dominate the cellular response, likely leading to a mitochondrial damage and apoptotic signaling previously reported in the literature [76]. The nearly identical viability values across both cell types throughout the concentration range highlight the need for further surface modification if selective targeting is desired. Overall, the data confirm these type of IONPs are safe at doses under 250 μg/mL, but may exert non-specific cytotoxicity at higher concentrations, a behavior consistent with previous literature on the biological impact of iron oxide nanomaterials [74–77].

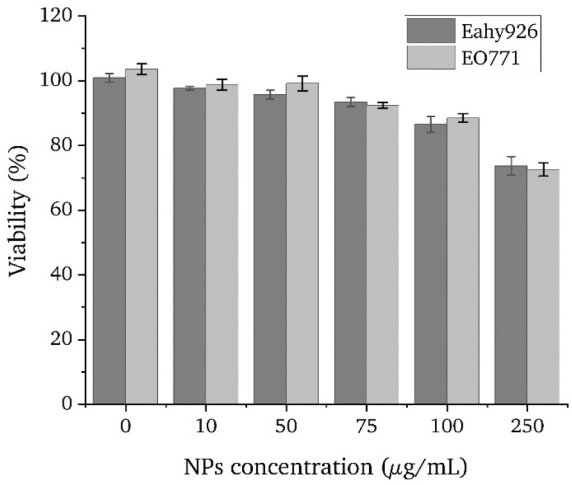

Fig. 10. Viability of Eahy926 and EO771 cells at selected NPs concentrations of sample G2N3S1.

4. Conclusions

We propose the present MWS method harnessing the formation of glycinates as intermediate complexes with a phase-director effect to produce IONPs in aqueous media. The formation of these glycinate complexes widens the stability range of iron species towards higher pH values, preventing an early triggering of the Schikorr reaction to form unwanted iron hydroxides that otherwise direct to uncontrollable reaction pathways. This is of utmost importance for MWS—where its frequent limitation to perform multi-stage reactions means that all the reagents are in contact from the beginning—, as it leads to shorter reaction times and better yields, which are some of the most anticipated qualities of this type of method. In addition to glycine, the dual glucose-fructose coating provides broader built-in functionality for targeting specific glucose and fructose receptors or transporters in cancer cells. Added to this are the possibilities of bioconjugation with relevant biomolecules—such as proteins, antibodies—offered by glycine. The exemplary IONPs assessed demonstrate good in vitro biocompatibility, maintaining over 85 % cell viability even at concentrations as high as 100 μg/mL. Overall, these results raise the possibility of extending this potentially scalable method to produce other biocompatible magnetic nanoparticle systems based on transition metal oxides.

CRediT authorship contribution statement

Antonio Santana-Otero: Writing – review & editing, Writing – original draft, Investigation, Formal analysis. **Carlos Frade-González:** Writing – review & editing, Writing – original draft, Investigation, Formal analysis, Conceptualization. **Milagrosa Ramírez-del-Solar:** Writing – review & editing, Supervision, Resources, Investigation, Formal analysis, Conceptualization. **Daniel Ortega:** Writing – review & editing, Writing – original draft, Supervision, Resources, Investigation, Funding acquisition, Formal analysis, Conceptualization.

Declaration of Competing Interest

The authors declare that they have no known competing financial interests or personal relationships that could have appeared to influence the work reported in this paper.

Acknowledgements

We acknowledge support under grants PID2020–117544RB-I00 and CEX2020–001039-S funded by MCIN/AEI/10.13039/501100011033,

and grant RYC2018–025253-I funded by MCIN/AEI/10.13039/501100011033 and by "FEDER A way of making Europe". We also thank the European COST action CA23132 (NexMPI). C. F. is grateful for a UCA/REC13VPCT/2020 FPI-UCA grant through the University of Cádiz. We are grateful for the support of the University of Cádiz through its Internal Research and Transfer Plan, as well as its Electron Microscopy Division included in the Science and Technology Research Central Services (SCI-CyT) of the university.

Appendix A. Supporting information

Supplementary data associated with this article can be found in the online version at doi:10.1016/j.jallcom.2025.181720.

Data availability

The data supporting the findings of this study are available from the corresponding author upon a reasonable request.

References

[1] M. Baghbanzadeh, L. Carbone, P.D. Cozzoli, C.O. Kappe, Microwave-assisted synthesis of colloidal inorganic nanocrystals, Angew. Chem. Int. Ed. 50 (2011) 11312–11359.
[2] N. Devi, S. Sahoo, R. Kumar, R.K. Singh, A review of the microwave-assisted synthesis of carbon nanomaterials, metal oxides/hydroxides and their composites for energy storage applications, Nanoscale 13 (2021) 11679–11711.
[3] M. Tsuji, M. Hashimoto, Y. Nishizawa, M. Kubokawa, T. Tsuji, Microwave-assisted synthesis of metallic nanostructures in solution, Chem. A Eur. J. 11 (2005) 440–452.
[4] H. Chen, K. Lv, Y. Du, H. Ye, D. Du, Microwave-assisted rapid synthesis of Fe2O3/ACF hybrid for high efficient As(V) removal, J. Alloy. Compd. 674 (2016) 399–405.
[5] Z. Luo, J. Quan, T. Ding, B. Xu, W. Li, Q. Mao, W. Ma, M. Li, H. Xiang, M. Zhu, Recent advances in iron oxide/graphene composites for flexible supercapacitors, J. Alloy. Compd. 980 (2024) 173614.
[6] L. Gonzalez-Moragas, S.-M. Yu, N. Murillo-Cremaes, A. Laromaine, A. Roig, Scale-up synthesis of iron oxide nanoparticles by microwave-assisted thermal decomposition, Chem. Eng. J. 281 (2015) 87–95.
[7] I. Rubia-Rodriguez, A. Santana-Otero, S. Spassov, E. Tombacz, C. Johansson, P. De La Presa, F.J. Teran, Puerto Morales, S. Veintemillas-Verdaguer, N.T.K. Thanh, M. O. Besenhard, C. Wilhelm, F. Gazeau, Q. Harmer, E. Mayes, B.B. Manshian, S. J. Soenen, Y. Gu, A. Millan, E.K. Efthimiadou, J. Gaudet, P. Goodwill, J. Mansfield, U. Steinhoff, J. Wells, F. Wiekhorst, D. Ortega, Whither magnetic hyperthermia? A tentative roadmap, Materials 14 (2021) 706.
[8] E.A. Osborne, T. Atkins, M, D.A. ilbert, S. Kauzlarich, M, K. Liu, A. Louie, Y, Rapid microwave-assisted synthesis of dextran-coated iron oxide nanoparticles for magnetic resonance imaging, Nanotechnology 23 (2012) 215602.
[9] C. Blanco-Andujar, D. Ortega, P. Southern, Q.A. Pankhurst, N.T.K. Thanh, High performance multi-core iron oxide nanoparticles for magnetic hyperthermia: microwave synthesis, and the role of core-to-core interactions, Nanoscale 7 (2015) 1768–1775.
[10] M.E.F. Brollo, S. Veintemillas-Verdaguer, C.M. Salvan, M.D.P. Morales, Key parameters on the microwave assisted synthesis of magnetic nanoparticles for mri contrast agents, Contrast Media Mol. Imaging 2017 (2017) 8902424.
[11] E. Carenza, V. Barceló, A. Morancho, J. Montaner, A. Rosell, A. Roig, Rapid synthesis of water-dispersible superparamagnetic iron oxide nanoparticles by a microwave-assisted route for safe labeling of endothelial progenitor cells, Acta Biomater. 10 (2014) 3775–3785.
[12] J. Mosayebi, M. Kiyasatfar, S. Laurent, Synthesis, functionalization, and design of magnetic nanoparticles for theranostic applications, Adv. Healthc. Mater. 6 (2017) 1700306.
[13] O. Pascu, E. Carenza, M. Gich, S. Estradé, F. Peiró, G. Herranz, A. Roig, Surface reactivity of iron oxide nanoparticles by microwave-assisted synthesis; comparison with the thermal decomposition route, J. Phys. Chem. C 116 (2012) 15108–15116.
[14] I. Bilecka, I. Djerdj, M. Niederberger, One-minute synthesis of crystalline binary and ternary metal oxide nanoparticles, Chem. Commun. (2008) 886–888.
[15] N. Janik-Olchawa, A. Drozdz, D. Ryszawy, M. Pudelek, K. Planeta, Z. Setkowicz, M. Sniegocki, M. Wytrwal-Sarna, M. Gajewska, J. Chwiej, The influence of IONPs core size on their biocompatibility and activity in in vitro cellular models, Sci. Rep. 11 (2021) 21808.
[16] J.-w Kim, J. Cheong, H. Cheong, J.G. Yoon, J.-Y. Jung, J.-H. Lee, T.-H. Shin, Iron oxide-coated dextran nanoparticles with efficient renal clearance for musculoskeletal magnetic resonance imaging, ACS Appl. Nano Mater. 4 (2021) 12943–12948.
[17] J. Li, Y. Liu, R. Cha, B. Ran, K. Mou, H. Wang, Q. Xie, J. Sun, X. Jiang, The biocompatibility evaluation of iron oxide nanoparticles synthesized by a one pot process for intravenous iron supply, RSC Adv. 6 (2016) 14329–14334.
[18] T. Liu, R. Bai, H. Zhou, R. Wang, J. Liu, Y. Zhao, C. Chen, The effect of size and surface ligands of iron oxide nanoparticles on blood compatibility, RSC Adv. 10 (2020) 7559–7569.
[19] S.A. Predoi, S.L. Iconaru, D. Predoi, In vitro and in vivo biological assays of dextran coated iron oxide aqueous magnetic fluids, Pharmaceutics 15 (2023) 177.
[20] N. Lee, D. Yoo, D. Ling, M.H. Cho, T. Hyeon, J. Cheon, Iron oxide based nanoparticles for multimodal imaging and magnetoresponsive therapy, Chem. Rev. 115 (2015) 10637–10689.
[21] L.H. Reddy, J.L. Arias, J. Nicolas, P. Couvreur, Magnetic nanoparticles: design and characterization, toxicity and biocompatibility, Pharm. Biomed. Appl. Chem. Rev. 112 (2012) 5818–5878.
[22] D. Ling, T. Hyeon, Chemical design of biocompatible iron oxide nanoparticles for medical applications, Small 9 (2013) 1450–1466.
[23] P. Choo, T. Liu, T.W. Odom, Nanoparticle shape determines dynamics of targeting nanoconstructs on cell membranes, J. Am. Chem. Soc. 143 (2021) 4550–4555.
[24] A. Tomitaka, H. Arami, S. Gandhi, K.M. Krishnan, Lactoferrin conjugated iron oxide nanoparticles for targeting brain glioma cells in magnetic particle imaging, Nanoscale 7 (2015) 16890–16898.
[25] K. Wilkinson, B. Ekstrand-Hammarström, L. Ahlinder, K. Guldevall, R. Pazik, L. Kępiński, K.O. Kvashnina, S.M. Butorin, H. Brismar, B. Önfelt, L. Österlund, G. A. Seisenbaeva, V.G. Kessler, Visualization of custom-tailored iron oxide nanoparticles chemistry, uptake, and toxicity, Nanoscale 4 (2012) 7383–7393.
[26] A.P. Khandhar, P. Keselman, S.J. Kemp, R.M. Ferguson, P.W. Goodwill, S. M. Conolly, K.M. Krishnan, Evaluation of PEG-coated iron oxide nanoparticles as blood pool tracers for preclinical magnetic particle imaging, Nanoscale 9 (2017) 1299–1306.
[27] G. Schikorr, Über die Reaktionen zwischen Eisen, Seinen Hydroxyden und Wasser, Zeitschrift für, Elektrochem. Angew. Phys. Chem. 35 (1929) 65–70.
[28] C.Q. Li, Z.M. Long, D.L. Guo, W.Y. Xie, L. Liu, Y.L. Ma, B. Shao, Catalytic mechanism of the Schikorr reaction promoted by the copper oxide nanosheet during a low-temperature hydrothermal process, Mater. Chem. Phys. 302 (2023) 127732.
[29] Selwyn,Overview archaeological iron corrosion problem key factors affecting treatment gaps current knowledge, in, Proceedings of Metal (2004) 294–306.
[30] F.J. Shipko, D.L. Douglas, Stability of ferrous hydroxide precipitates, J. Phys. Chem. Us 60 (1956) 1519–1523.
[31] U.R. Evans, J.N. Wanklyn, Evolution of hydrogen from ferrous hydroxide, Nature 162 (1948) 27–28.
[32] M. Regel-Rosocka, A review on methods of regeneration of spent pickling solutions from steel processing, J. Hazard Mater. 177 (2010) 57–69.
[33] M. Ma, Y. Zhang, Z. Guo, N. Gu, Facile synthesis of ultrathin magnetic iron oxide nanoplates by Schikorr reaction, Nanoscale Res. Lett. 8 (2013) 16.
[34] M. Yamamoto, Y. Takamura, Y. Kokubo, M. Urushihara, N. Horiuchi, W. Dai, Y. Hayasaka, E. Kita, K. Takao, Solid-state schikorr reaction from ferrous chloride to magnetite with hydrogen evolution as the kinetic bottleneck, Inorg. Chem. 62 (2023) 14580–14589.
[35] J.P. Buchmann, E.C. Holmes, Cell walls and the convergent evolution of the viral envelope, Microbiol. Mol. Biol. Rev. 79 (2015) 403–418.
[36] Y. Chevolot, S. Vidal, E. Laurenceau, F. Morvan, J.-J. Vasseur, E. Souteyrand, Carbohydrates as Recognition Receptors in Biosensing Applications, in: M. Zourob (Ed.), Recognition Receptors in Biosensors, Springer New York, New York, NY, 2010, pp. 275–341.
[37] G. Cotin, C. Blanco-Andujar, F. Perton, L. Asín, J.M. de la Fuente, W. Reichardt, D. Schaffner, D.-V. Ngyen, D. Mertz, C. Kiefer, F. Meyer, S. Spassov, O. Ersen, M. Chatzidakis, G.A. Botton, C. Hénoumont, S. Laurent, J.-M. Greneche, F.J. Teran, D. Ortega, D. Felder-Flesch, S. Begin-Colin, Unveiling the role of surface, size, shape and defects of iron oxide nanoparticles for theranostic applications, Nanoscale 13 (2021) 14552–14571.
[38] A. Demir, R. Topkaya, A. Baykal, Green synthesis of superparamagnetic Fe3O4 nanoparticles with maltose: its magnetic investigation, Polyhedron 65 (2013) 282–287.
[39] A. Omelyanchik, A.S. Kamzin, A.A. Valiullin, V.G. Semenov, S.N. Vereshchagin, M. Volochaev, A. Dubrovskiy, T. Sviridova, I. Kozenkov, E. Dolan, D. Peddis, A. Sokolov, V. Rodionova, Iron oxide nanoparticles synthesized by a glycine-modified coprecipitation method: structure and magnetic properties, Colloids Surf. A Physicochem. Eng. Asp. 647 (2022) 129090.
[40] M. Racuciu, L. Barbu-Tudoran, S. Oancea, O. Draghici, C. Morosanu, M. Grigoras, F. Brinza, D.E. Creanga, Aspartic acid stabilized iron oxide nanoparticles for biomedical applications, Nanomaterials 12 (2022) 1151.
[41] X. Sun, C. Zheng, F. Zhang, Y. Yang, G. Wu, A. Yu, N. Guan, Size-controlled synthesis of magnetite (Fe3O4) nanoparticles coated with glucose and gluconic acid from a single Fe(III) precursor by a sucrose bifunctional hydrothermal method, J. Phys. Chem. C 113 (2009) 16002–16008.
[42] V. Vacchina, S. Oguey, C. Ionescu, D. Bravo, R. Lobinski, Characterization of metal glycinate complexes by electrospray Q-TOF-MS/MS and their determination by capillary electrophoresis-ICP-MS: application to premix samples, Anal. Bioanal. Chem. 398 (2010) 435–449.
[43] K. Micskei, I. Nagypál, Kinetic studies in aqueous solutions of iron(II)-glycinate, -ethylenediamine, and -malonate complexes, J. Chem. Soc. Dalton Trans. (1990) 743–747.
[44] V. Cuculić, I. Pižeta, Kinetics of iron (III) hydrolysis and precipitation in aqueous glycine solutions assessed by voltammetry, Collect. Czechoslov. Chem. Commun. 74 (2009) 1531–1542.
[45] G. Eshova, J. Davlatshoeva, M. Rakhimova, M. Guriev, L. Kvyatkovskaya, Formation of glycinate complexes of iron (II) at different ionic strengths of solution, Russ. J. Inorg. Chem. 63 (2018) 772–776.
[46] T. Degen, M. Sadki, E. Bron, U. König, G. Nénert, The highscore suite, Powder Diffr. 29 (2014) S13–S18.

[47] W.E. Wallace, Infrared Spectra by NIST Mass Spectrometry Data Center, in: Infrared Spectra by NIST Mass Spectrometry Data Center, NIST Interagency/ Internal Report (NISTIR), NIST, Gaithersburg, 2022.
[48] B.D. Cullity, C.D. Graham, Introduction to magnetic materials, John Wiley & Sons, 2011.
[49] S. Bernal, F.J. Botana, J.J. Calvino, C. López-Cartes, J.A. Pérez-Omil, J.M. Rodríguez-Izquierdo, The interpretation of HREM images of supported metal catalysts using image simulation: profile view images, Ultramicroscopy 72 (1998) 135–164.
[50] C.N. Johnstone, A. Chand, T.L. Putoczki, M. Ernst, Emerging roles for IL-11 signaling in cancer development and progression: focus on breast cancer, Cytokine Growth Factor Rev. 26 (2015) 489–498.
[51] J.J. Arroyo-Crespo, A. Arminan, D. Charbonnier, C. Deladriere, M. Palomino-Schatzlein, R. Lamas-Domingo, J. Forteza, A. Pineda-Lucena, M.J. Vicent, Characterization of triple-negative breast cancer preclinical models provides functional evidence of metastatic progression, Int J. Cancer 145 (2019) 2267–2281.
[52] C.J. Edgell, C.C. McDonald, J.B. Graham, Permanent cell line expressing human factor VIII-related antigen established by hybridization, Proc. Natl. Acad. Sci. 80 (1983) 3734–3737.
[53] S. Wilhelm, A.J. Tavares, Q. Dai, S. Ohta, J. Audet, H.F. Dvorak, W.C.W. Chan, Analysis of nanoparticle delivery to tumours, Nat. Rev. Mater. 1 (2016) 16014.
[54] A.K. Brisdon, UV-Visible Spectroscopy, Inorganic Spectroscopic Methods. Oxford: Oxford UP, (1998) 70-73.
[55] I. Fontana, A. Lauria, G. Spinolo, Optical absorption spectra of Fe2+ and Fe3+ in aqueous solutions and hydrated crystals, Phys. Status Solidi 244 (b) (2007) 4669–4677.
[56] S. Ge, X. Shi, K. Sun, C. Li, C. Uher, J.R. Baker Jr., M.M. Banaszak Holl, B.G. Orr, Facile hydrothermal synthesis of iron oxide nanoparticles with tunable magnetic properties, J. Phys. Chem. C. 113 (2009) 13593–13599.
[57] C.P. Marshall, W.J.B. Dufresne, C.J. Rufledt, Polarized Raman spectra of hematite and assignment of external modes, J. Raman Spectrosc. 51 (2020) 1522–1529.
[58] I. Chamritski, G. Burns, Infrared- and raman-active phonons of magnetite, maghemite, and hematite: a computer simulation and spectroscopic study, J. Phys. Chem. B 109 (2005) 4965–4968.
[59] L.E. Semenova, K.A. Prokhorov, Theoretical analysis of resonant Raman scattering by 2LO phonons, J. Raman Spectrosc. 32 (2001) 942–946.
[60] E. Wiercigroch, E. Szafraniec, K. Czamara, M. Pacia, Z, K. Majzner, K. Kochan, A. Kaczor, M. Baranska, K. Malek, Raman and infrared spectroscopy of carbohydrates: a review, Spectrochim. Acta Part A Mol. Biomol. Spectrosc. 185 (2017) 317–335.
[61] K. Kozlowicz, R. Rozylo, B. Gladyszewska, A. Matwijczuk, G. Gladyszewski, D. Chocyk, K. Samborska, J. Piekut, M. Smolewska, Identification of sugars and phenolic compounds in honey powders with the use of GC-MS, FTIR spectroscopy, and X-ray diffraction, Sci. Rep. 10 (2020) 16269.
[62] M. Ishii, M. Nakahira, T. Yamanaka, Infrared absorption spectra and cation distributions in (Mn, Fe)3O4, Solid State Commun. 11 (1972) 209–212.
[63] L.V. Gasparov, D.B. Tanner, D.B. Romero, H. Berger, G. Margaritondo, L. Forró, Infrared and Raman studies of the Verwey transition in magnetite, Phys. Rev. B 62 (2000) 7939–7944.
[64] N. Naveas, R. Pulido, C. Marini, P. Gargiani, J. Hernandez-Montelongo, I. Brito, M. Manso-Silván, First-principles calculations of magnetite (Fe3O4) above the verwey temperature by using self-consistent DFT + U + V, J. Chem. Theory Comput. 19 (2023) 8610–8623.
[65] J.M.D. Coey, Magnetic Oxides and Other Compounds, in: J.M.D. Coey, S.S. P. Parkin (Eds.), Handbook of Magnetism and Magnetic Materials, Springer International Publishing, Cham, 2021, pp. 847–922.
[66] J.M.D. Coey, Noncollinear spin arrangement in ultrafine ferrimagnetic crystallites, Phys. Rev. Lett. 27 (1971) 1140–1142.
[67] X. Guan, G. Zhou, W. Xue, Z. Quan, X. Xu, The investigation of giant magnetic moment in ultrathin Fe3O4 films, APL Mater 4 (2016) 036104.
[68] D. Zákutná, D. Nižňanský, L.C. Barnsley, E. Babcock, Z. Salhi, A. Feoktystov, D. Honecker, S. Disch, Field dependence of magnetic disorder in nanoparticles, Phys. Rev. X 10 (2020) 031019.
[69] H. Kachkachi, D.A. Garanin, in: D. Fiorani (Ed.), Magnetic Nanoparticles as Many-Spin Systems, Surface Effects in Magnetic Nanoparticles, Springer US, Boston, MA, 2005, pp. 75–104.
[70] J. Mohapatra, F. Zeng, K. Elkins, M. Xing, M. Ghimire, S. Yoon, S.R. Mishra, J. P. Liu, Size-dependent magnetic and inductive heating properties of Fe3O4 nanoparticles: scaling laws across the superparamagnetic size, Phys. Chem. Chem. Phys. 20 (2018) 12879–12887.
[71] E. Lysenko, A. Surzhikov, E. Nikolaev, O. Starý, Curie Temperature Control of Magnetic Materials Using Thermogravimetric Measurements in Magnetic Field, in: E. Lysenko, A. Rogachev, O. Starý (Eds.), Recent Developments in the Field of Non-Destructive Testing, Safety and Materials Science, Springer International Publishing, Cham, 2023, pp. 195–203.
[72] U. Schwertmann, R.M. Cornell, Iron oxides in the laboratory: preparation and characterization, John Wiley & Sons, 2008.
[73] ISO 10993-5:2009, Biological evaluation of medical devices—part 5: tests for in vitro cytotoxicity, International Organization for Standardization, Geneva, Switzerland, 2009.
[74] A.K. Gupta, M. Gupta, Synthesis and surface engineering of iron oxide nanoparticles for biomedical applications, Biomaterials 26 (2005) 3995–4021.
[75] S. Laurent, D. Forge, M. Port, A. Roch, C. Robic, L. Vander Elst, R.N. Muller, Magnetic iron oxide nanoparticles: synthesis, stabilization, vectorization, physicochemical characterizations, and biological applications, Chem. Rev. 108 (2008) 2064–2110.
[76] N. Singh, B. Manshian, G.J. Jenkins, S.M. Griffiths, P.M. Williams, T.G. Maffeis, C. J. Wright, S.H. Doak, NanoGenotoxicology: the DNA damaging potential of engineered nanomaterials, Biomaterials 30 (2009) 3891–3914.
[77] M. Mahmoudi, S. Sant, B. Wang, S. Laurent, T. Sen, Superparamagnetic iron oxide nanoparticles (SPIONs): development, surface modification and applications in chemotherapy, Adv. Drug Deliv. Rev. 63 (2011) 24–46.